

Splat-Nav: Safe Real-Time Robot Navigation in Gaussian Splatting Maps

Timothy Chen¹, Ola Shorinwa¹, Weijia Zeng², Joseph Bruno³, Philip Dames³, Mac Schwager¹

Abstract—We present Splat-Nav, a navigation pipeline that consists of a real-time safe planning module and a robust state estimation module designed to operate in the Gaussian Splatting (GSplat) environment representation, a popular emerging 3D scene representation from computer vision. We formulate rigorous collision constraints that can be computed quickly to build a guaranteed-safe polytope corridor through the map. We then optimize a B-spline trajectory through this corridor. We also develop a real-time, robust state estimation module by interpreting the GSplat representation as a point cloud. The module enables the robot to localize its global pose with zero prior knowledge from RGB-D images using point cloud alignment, and then track its own pose as it moves through the scene from RGB images using image-to-point cloud localization. All of these modules operate mainly on CPU, freeing up GPU resources for tasks like real-time scene reconstruction. We demonstrate the safety and robustness of our pipeline in both simulation and hardware, where we show re-planning at 5 Hz and pose estimation at 20 Hz, an order of magnitude faster than Neural Radiance Field (NeRF)-based navigation methods, thereby enabling real-time navigation.

I. INTRODUCTION

Constructing a representation of the environment from data collected by onboard sensors, such as RGB(-D) cameras, lidar, or touch sensors, is a fundamental challenge for any autonomous system. Traditionally, these representations have included (watertight) triangular meshes [7], occupancy grids [8], point clouds [21], and Signed Distance Fields (SDFs) [33]. In each of these situations, the geometry is well-defined and there are many methods for planning and localizing within these maps.

Neural Radiance Fields (NeRFs) [30] have recently emerged in the computer vision community as a promising 3D scene representation. NeRFs offer several potential benefits over traditional scene representations: they provide photo-realistic renderings, they can be trained using only monocular RGB images, and current implementations can train NeRFs in seconds [31, 43]. However, NeRFs implicitly represent the environment as a volumetric density using a multilayer perceptron (MLP) deep neural network. This makes scene rendering of the environment computationally expensive and makes it difficult to use NeRFs for standard robotics tasks in an interpretable

*This work was supported in part by ONR grant N00014-23-1-2354 and DARPA grant HR001120C0107 and NSF grant 2220866. Toyota Research Institute provided funds to support this work. The first author was supported by a NASA NSTGRO Fellowship.

¹ Stanford University, Stanford, CA 94305, USA {chengine, shorinwa, schwager}@stanford.edu

²University of California San Diego, San Diego, CA 92093, USA, wez195@ucsd.edu

³Temple University, Philadelphia, PA 19122, USA, {brunoj6, pdames}@temple.edu

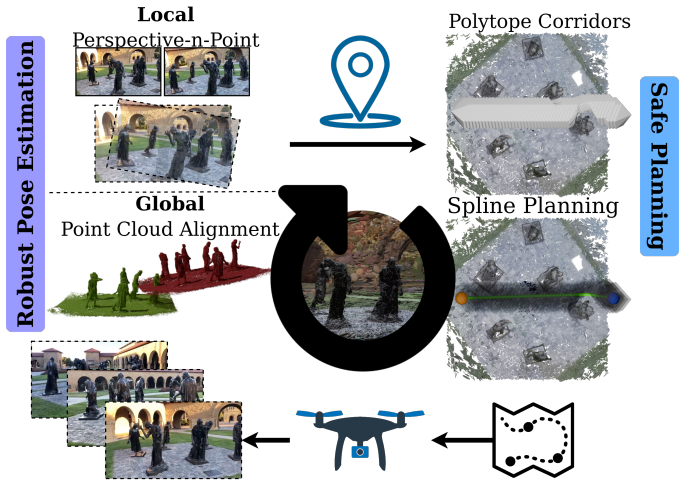


Fig. 1. Our real-time, robust navigation pipeline, Splat-Nav, consists of a safe planning module, Splat-Plan, and robust localization module, Splat-Loc, both powered by the Gaussian Splatting environment representation. We first represent our agent as an ellipsoid, and then rapidly solve for smooth paths using an ellipsoid-to-ellipsoid collision test. We then use the point cloud representation from the Gaussian Splat map to perform both global camera localization from RGB(-D) images using point cloud alignment, and online pose tracking using only RGB images with a PnP image-to-point cloud pose refinement. Additionally, we also learn a semantic channel to direct the robot towards regions of space that benefit the localization.

way, especially for tasks that require interacting with the environment.

More recently, Gaussian Splatting (GSplat) [20] has emerged as an expressive scene representation and differentiable rendering pipeline, trained from RGB images. GSplat represents the environment as a union of ellipsoidal objects, learning the number of ellipsoids along with the position, extents, color, and opacity of each. This approach allows for faster reconstruction by taking advantage of fast differential rasterization techniques for 3D Gaussians on the GPU and often yields more photorealistic renderings compared to NeRFs. More importantly for robotics, the use of (convex) geometric primitives facilitates the development of rigorous motion planning algorithms that are safe, robust, and real-time.

In this paper, we develop a framework called Splat-Nav, outlined in Fig. 1, for robot trajectory planning and pose estimation that is intertwined with the GSplat representation. The first component, Splat-Plan, generates safe trajectories through the GSplat scene. The primary contribution is a

computationally efficient collision checker that is guaranteed to be safe. We demonstrate the flexibility of this checker by using it within two different motion planners: a sampling-based planner (RRT) [24] and a spline generation method [27]. We believe the theory presented in this work may also be useful for other planning methods as well as downstream applications built on Gaussian Splatting.

The second component, Splat-Loc, allows the robot to localize itself within the GSplat map using images from its onboard camera. The primary contribution is interpreting the GSplat map as a point cloud with features including the color and opacity values. Using this observation, we can use robust, off-the-shelf point cloud alignment algorithms to perform global pose alignment with zero prior pose knowledge (i.e., the kidnapped robot problem). We then perform real-time local image-to-point cloud pose estimation for the robot to track its motion through the scene, leveraging the high rendering speed of Gaussian Splatting. Both these modules are many times faster than their existing neural network-based NeRF counterparts, which do not provide guarantees on performance [1].

To showcase these two modules, we provide simulation and hardware results to show that our pipeline: (1) generates safe, but not conservative, trajectories through the environment, (2) robustly localizes a robot in the scene, and (3) can be executed in real-time. We contrast our paths to those generated from prior work [1] that used NeRFs as the scene representation and to other baselines. Our planner demonstrates generalizable safe behavior and is not conservative. We also contrast localization results from the same work. We find that our localization is more accurate, much faster, and fails less often. We demonstrate re-planning at 5 Hz and online pose estimation at 20 Hz on a desktop computer, enabling real-time navigation.

II. RELATED WORK

Here, we review the related literature in robot planning and localization with different map representations, which we categorize into three groups: traditional representations (e.g., occupancy grids, meshes, point clouds, and SDFs), NeRFs, and GSplat.

A. Traditional Map Representations

1) *Planning*: There is a long history of planning within robotics. LaValle [22] provides an excellent explanation of the major algorithms in this realm. Most relevant for this work are the graph-based planners (e.g., A*), which compute a path over a grid representation of the environment; sampling-based planners (e.g., PRM [19], RRT [23], and RRT* [17]), which generate a path by sampling candidate states within the configuration space of the robot; and trajectory optimization-based planners (e.g. CHOMP [35] and Traj-Opt [39]), which take an optimization-based approach to planning. The Open Motion Planning Library (OMPL) [40] provides open-source implementations of many of these algorithms, which we use later for both path initialization and benchmarking. Liu et al. [27] utilizes an optimization-based approach in path planning,

taking a point cloud representation of the environment and converting this into a set of safe polytopes. The resulting safe polytopes are utilized in computing a safe trajectory, parameterized as a spline, from a quadratic program (QP), which can be efficiently solved.

There is also extensive literature on planning based on onboard sensing. Typically, these works present reactive control schemes [48, 49, 50], using the sensed depth directly to perform collision checking in real-time. These methods typically are myopic, reasoning only locally about the scene. Consequently, such methods often converge to local optima in many problems, hindering the robot from reaching its goal, especially in cluttered/intricate environments. An alternate approach is to construct a map of the environment using the depth measurements. Often, a Signed Distance Field (SDF) or its truncated variant (TSDF) is constructed from depth data [32, 13], which is often encoded within a voxel representation. Such a representation is typical in dynamic robotic motion planning, providing fast collision checking and gradients in planning.

2) *Localization*: Prior work in robot localization utilize filtering schemes, such as Extended Kalman Filters (EKFs) [12, 9], Particle Filters (PFs) [10, 54], and other related filters [46, 2], to solve the pose localization problem. These methods generally estimate the pose of the robot from low-dimensional observations (measurements), extracted from the high-dimensional observations collected by the robot’s on-board sensors, such as cameras. This approach often fails to leverage the entire information available in the raw, high-dimensional measurements. Learning-based filtering methods [18, 16, 42] seek to address this limitation using deep-learning to develop end-to-end frameworks for localization, computing a pose estimate directly from raw camera images. Although learning-based approaches can be quite effective given sufficient training data, these methods are often limited to a single robot platform (dynamics model), and thus require separate filters for each robot or environment.

B. NeRF Maps

1) *Planning*: NeRFs implicitly represent the environment as a spatial density field (with color) [30]. There are a number of works on planning in this representation. Adamkiewicz et al. [1] plan trajectories for differentially flat robots, such as quadrotors, that minimize a total collision cost. Chen et al. [3] convert the NeRF into a probabilistic voxel grid and then use this to generate trajectories parameterized as Bézier curves. Tong et al. [45] uses the predicted depth map at sampled poses to enforce step-wise safety using a control barrier function. The above works are complementary, with Adamkiewicz et al. [1], Chen et al. [3] serving as high-level planners that encourage non-myopic behavior while Tong et al. [45] can be used as a safety filter for a myopic low-level controller.

2) *Localization*: There is some existing work on tracking the pose of a robot equipped with an on-board camera and IMU through a pre-trained NeRF map. iNeRF [52] does this

for single images, and NeRF-Nav [1] and Loc-NeRF [28] both track a trajectory using a sequence of images. Other works consider simultaneous localization and mapping (SLAM) using a NeRF map representation. Sucar et al. [41], Yen-Chen et al. [52], Zhu et al. [55] all simultaneously optimize the NeRF weights and the robot/camera poses. Rosinol et al. [36] propose a combination of an existing visual odometry pipeline for camera trajectory estimation together with online NeRF training for the 3D scene.

C. GSplat Maps

To the best of our knowledge, there are no planning algorithms designed to operate in GSplat environments. There are a few recent works on SLAM using a GSplat representation of the environment [51, 53, 29]. However, none of these works have a standalone real-time pose localization component.

III. PLANNING

Now we present our planning pipeline based on Gaussian Splatting, called Splat-Plan. The pipeline consists of generating safe polytopic corridors (inspired by [27]) that discretizes the free space of a GSplat, rigorously built on theory derived from tests for intersection between ellipsoids. The method is also fast enough to provide real-time operation, provides generalizable safety guarantees, and is not conservative.

A. Problem Statement

Our approach leverages the ellipsoidal representation of objects in a GSplat. An ellipsoid \mathcal{E}_j is parameterized by covariance Σ_j and mean μ_j :

$$\mathcal{E}_j = \{x \in \mathbb{R}^3 \mid (x - \mu_j)^T \Sigma_j^{-1} (x - \mu_j) \leq 1\}. \quad (1)$$

Given a bounding ellipsoid $\mathcal{E}_{\mathcal{R}}$ for the robot and a union of N ellipsoids $\mathcal{G} = \{\mathcal{E}_j\}_{j=1}^N$ (from GSplat), we seek to find a feasible path from an initial position X to a goal position Y such that there are no collisions, i.e., $\mathcal{E}_{\mathcal{R}} \cap \mathcal{E}_j = \emptyset, \forall \mathcal{E}_j \in \mathcal{G}$.

B. Minimal Bounding Ellipsoid

Typically, robots are represented by a point cloud or a mesh. A mesh of M vertices can be converted to a point cloud by selecting its vertices to yield $\mathcal{P}_{\mathcal{R}} = \{x_i\}_{i=1}^M$. In order to convert these canonical representations to the one we desire, we can solve a simple convex program to generate our ellipsoid $\mathcal{E}_{\mathcal{R}}$. To do this, we solve the following convex program:

$$\begin{aligned} & \text{minimize}_{A,b} -\log |A| \\ & \text{subject to} \\ & \quad \|Ax_i + b\|_2 \leq 1, \forall x_i \in \mathcal{P}_{\mathcal{R}}. \end{aligned} \quad (2)$$

Then, the mean of $\mathcal{E}_{\mathcal{R}}$ is given by $\mu_{\mathcal{R}} = -A^{-1}b$ and the covariance $\Sigma_{\mathcal{R}} = (A^T A)^{-1}$. Note, if the robot body consists of many points, computing the convex hull of these points first, and using the convex hull vertices in (2) will drastically lower the computation costs.

C. Collision Detection

The environment and the robot body are represented completely by ellipsoids or unions thereof. Therefore, collision is identical to finding intersection between two ellipsoids (the robot body and an ellipsoid \mathcal{E}_j from the environment). This is given by the following Theorem.

Theorem 1. Consider two ellipsoid $\mathcal{E}_a, \mathcal{E}_b$ (with means μ_a, μ_b and covariances Σ_a, Σ_b) and the concave scalar function $K : (0, 1) \rightarrow \mathbb{R}$,

$$K(s) = (\mu_b - \mu_a)^T \left[\frac{1}{1-s} \Sigma_a + \frac{1}{s} \Sigma_b \right]^{-1} (\mu_b - \mu_a).$$

Then, $\mathcal{E}_a \cap \mathcal{E}_b = \emptyset$ if and only if there exists $s \in (0, 1)$ such that $K(s) > 1$.

The proof for this is stated in Proposition 2 in Gilitschenski and Hanebeck [11]. Note that while K is concave in s (i.e., $-K$ is convex in s), it is *not* concave with respect to the means and variances.

Theorem 1 is a complete test that will always indicate whether two ellipsoids are in collision or not, however it is not computationally easy to solve. Although the existence of an s can be solved by maximizing the concave function K and asserting negativity, such a routine can be expensive for the many checks that must happen between the robot body and the environment since it involves a matrix inversion. To remedy this issue, we eliminate the matrix inversion by operating in a shared basis for both Σ_A and Σ_B .

Proposition 1. By solving the generalized eigenvalue problem for Σ_a and Σ_b , we obtain generalized eigenvalues λ_i and the corresponding matrix of generalized eigenvectors ϕ . Letting $v = \phi^T(\mu_a - \mu_b)$, Theorem 1 can then be simplified to

$$K(s) = v^T \text{diag} \left(\frac{s(1-s)}{1+s(\lambda_i-1)} \right) v.$$

Proof. This proposition was stated by [15], but there was no proof. We write the proof explicitly here. The goal is to diagonalize both Σ_a and Σ_b in such a way that they share the same eigenbasis. In this way, the matrix inversion amounts to a reciprocal of the eigenvalues. We can find such an eigenbasis through the generalized eigenvalue problem, which solves the following system of equations

$$\Sigma_a \phi_i = \lambda_i \Sigma_b \phi_i.$$

These generalized eigenvalues and eigenvectors satisfy the identity

$$\Sigma_a \phi = \Sigma_b \phi \Lambda.$$

To solve the generalized eigenvalue problem, we utilize the fact that Σ_a and Σ_b are symmetric, positive-definite, so the Cholesky decomposition of $\Sigma_b = LL^T$, where L is lower triangular. This also means that we can represent Σ_a by construction as

$$\Sigma_a = LCL^T = L\Lambda L^T,$$

where C is also symmetric, positive-definite, so its eigen-decomposition is $C = V\Lambda V^T$, where the eigenvectors V are orthonormal $V^T V = I$. To retrieve the original eigenbasis ϕ , we solve the triangular system $L^T \phi = V$. A consequence of this solution is that

$$V^T V = \phi^T L L^T \phi = \phi^T \Sigma_b \phi = I.$$

Moreover, this means that $\Sigma_b = \phi^{-T} \phi^{-1}$. We can show that Λ and ϕ indeed solve the generalized eigenvalue problem through the following substitution

$$\Sigma_a \phi = L V \Lambda V^T L^T \phi = \underbrace{L L^T}_{\Sigma_b} \phi \Lambda \phi^T \underbrace{L L^T}_{\Sigma_b} \phi = \Sigma_b \phi \Lambda \underbrace{\phi^T \Sigma_b \phi}_{I},$$

where $\Lambda = \text{diag}(\lambda_i)$ is the diagonal matrix of eigenvalues.

As a result, we can write the matrix inversion in Theorem 1 as the following

$$\begin{aligned} \left[\frac{1}{1-s} \Sigma_a + \frac{1}{s} \Sigma_b \right]^{-1} &= \left[\frac{1}{1-s} \Sigma_b \phi \Lambda \phi^T \Sigma_b + \frac{1}{s} \Sigma_b \right]^{-1} \\ &= \left[\phi^{-T} \left(\frac{1}{1-s} \Lambda + \frac{1}{s} I \right) \phi^{-1} \right]^{-1} \\ &= \phi \left[\frac{1}{1-s} \Lambda + \frac{1}{s} I \right]^{-1} \phi^T \\ &= \phi \text{diag} \left(\frac{s(1-s)}{1+s(\lambda_i-1)} \right) \phi^T. \end{aligned}$$

Multiplying the left and right by $\mu_b - \mu_a$ completes the proof. \square

Corollary 1. *A finite number of samples for $s \in (0, 1)$ will always find the presence of ellipsoid intersections. Hence, sampling instead of analytically solving Theorem 1 will still always yield safe behavior.*

Proof. Using a finite number of samples, the test can fail (no sample points yield $K(s) > 1$) or succeed (there is a sample point such that $K(s) > 1$). Should the test succeed, by definition, there is no intersection. If it fails, there either exists an un-sampled point with $K(s) > 1$ or such a point does not exist. If no such point exists, then the test remains correct in predicting collision. If such a point exists, it simply means our test predicted collision while in reality the ellipsoids are intersection-free. In other words, using finite samples leads to a safe, but conservative test. Due to the concavity of $K(s)$, more samples will asymptotically decrease the conservativeness. \square

The intersection test from Proposition 1 can now be parallelized by sampling many points between 0 and 1 and finding if any yield $K(s) > 1$. This operation can also be parallelized across batches of ellipsoids, leading to massive computation speedups.

Corollary 2. *Scaling the ellipsoids $\mathcal{E}_a, \mathcal{E}_b$ in Proposition 1 by a uniform positive scale factor α effectively scales $K(s)$ by a factor of $1/\alpha$.*

In the case of uncertainty, either in the state of the agent or the confidence in the Gaussian Splatting representation, a margin of safety is needed in order for experiments outside of simulation to be correct. We can scale the representation and/or the robot body according to Corollary 2 to achieve the desired safety margins.

Corollary 3. *Gaussian Splatting parametrizes the covariance of the j th ellipsoid as $\Sigma_j = R S S^T R^T$, where R^T is an orthonormal matrix that rotates the world coordinates into a body aligned frame, and S is a diagonal matrix representing the axes lengths. Let $S S^T = \text{diag}(\lambda_i)$ and let $w = R^T(\mu_R - \mu_j)$. In addition, if we choose to parameterize our robot body as a sphere with covariance $\Sigma_R = \kappa I$ then the intersection test can be simplified to*

$$K(s) = w^T \text{diag} \left(\frac{s(1-s)}{\kappa + s(\lambda_i - \kappa)} \right) w.$$

Note that this test is faster to query than in Proposition 1 as there is no need to perform an eigenvalue decomposition. This again has computation speedups. For non-spherical robots, one can approximate it as a sphere by setting κ to be the maximum eigenvalue of Σ_R (i.e., $\kappa = \lambda_{\max}(\Sigma_R)$).

D. Finding a Small Test Set

Although performing the collision test in Corollary 3 is fast, it is difficult to naively scale to test all ellipsoids in the scene (which is often in the 10's or 100's of thousands for GSplat maps) while maintaining real-time performance in a planner. As a result, we rely on the cost-effectiveness of KD-tree queries in our proposed algorithm to quickly converge on a small set of ellipsoids to test.

Algorithm 1: Minimal Collision Test Set

```

Input: Query point  $x$ , robot's largest eigenvalue  $\kappa$ , ellipsoids  $\mathcal{G} = \{\mu_i, \Sigma_i\}_{i=1}^N$ ;
Output: Minimal Collision Set  $\mathcal{G}_x \subseteq \mathcal{G}$ ;
 $\lambda_{\max}(\mathcal{I}) \triangleq \max_{i \in \mathcal{I}} \lambda_{\max}(\Sigma_i)$ ;
 $\text{KD} \leftarrow \text{KDTree}(\{\mu_i\})$ ;
 $\mathcal{I}_0 \leftarrow \{1, \dots, N\}$ ;
 $\mathcal{I}_1 \leftarrow \text{KD.QueryBallPoint}(x, \lambda_{\max}(\mathcal{I}_0) + \kappa)$ ;
while  $\lambda_{\max}(\mathcal{G}_1) < \lambda_{\max}(\mathcal{I}_0)$  or  $\mathcal{I}_1 \neq \emptyset$  do
|  $\mathcal{I}_0 \leftarrow \mathcal{I}_1$  ;
|  $\mathcal{I}_1 \leftarrow \text{KD.QueryBallPoint}(x, \lambda_{\max}(\mathcal{I}_0) + \kappa)$ ;
end
 $\mathcal{G}_x = \{\mu_i, \Sigma_i\}_{i \in \mathcal{I}_1}$ ;

```

The minimal collision test set \mathcal{G}_x is a ball centered at a test point x with a radius that guarantees the ball will contain the center of the largest ellipsoid (with largest eigenvalue λ_{\max}) whose circumscribed circle intersects with the robot body centered at x . We know for certain that ellipsoids outside of this ball cannot intersect with the robot body. We also know that necessarily, this ball must have radius at most $\lambda_{\max} + \kappa$, meaning the center of this ellipsoid lies on the surface of the ball. To find this minimal test set, we propose using Algorithm

1. We stop iterating when the largest eigenvalue between successive queries to the KD-tree does not change, meaning the ellipsoid corresponding with the largest eigenvalue is the largest ellipsoid that could intersect our robot. The algorithm will only find the minimal set if the center associated with λ_{\max} lies on the surface of the ball. However, the gap between the converged set and the minimal set is relatively small.

E. Supporting Hyperplanes

We like to again emphasize that having convex primitives (ellipsoids) as an environment representation facilitates development of interpretable algorithms. In this work, it is the ability to create polytopes that describe the safe regions of space through the use of supporting hyperplanes. Our contribution is inspired by [27]. However, there are two key differences. Liu et al. [27] assumes a point cloud as the environment, and requires an initial, safe path to create the polytopes. On the other hand, the safe polytopes generated using a GSplat are *generalizable*. Assuming a valid safe polytope exists, they can be generated by any sequence of points regardless of whether the points are in collision.

Proposition 2. *Given a test point x^* (i.e., robot position μ_R) and a collision test set \mathcal{G}^* , for every ellipsoid in \mathcal{G}^* , a supporting hyperplane to the j -th ellipsoid (considering the extent of the robot body) derived from Proposition 1 is given by*

$$\underbrace{\Delta_j^T Q_j x}_{a_j} \geq \underbrace{\frac{k_j^*}{1+\epsilon} + \Delta_j^T Q_j \mu_j}_{b_j},$$

for any $\epsilon > 0$ where $\Delta_j = x^* - \mu_j$, $s^* = \arg \max_{s \in (0,1)} K(s)$, $Q_j = \phi \text{ diag} \left(\frac{s^*(1-s^*)}{1+s^*(\lambda_i-1)} \right) \phi^T$, and $(k_j^*)^2 = K(s^*) = \Delta_j^T Q_j \Delta_j > 0$. Note that Q_j is always symmetric, positive-definite. By stacking the hyperplane constraints (a_j, b_j) , we arrive at a polytope $Ax \geq b$ that is guaranteed to be safe.

Proof. From Proposition 1, we know that we must find an x such that $K(s) > 1$ for all ellipsoids in the test set \mathcal{G}^* . We will approximate this safe set as a polytope. Given a test point x^* and the j th ellipsoid in the collision test set \mathcal{G}^* , we can use our collision test (Corollary 3) to derive these polytopes. Notice in (3) that μ_a represents the position of the robot (i.e., the test point x^*) and μ_b is the centroid of ellipsoid j . Once we find the value s^* that maximizes $K(s)$, the safety test is a quadratic constraint of the test point x^* , namely $\Delta_j^T Q_j \Delta_j > 1$.

To derive the supporting hyperplane for the safety check, we will first find the point on the ellipsoid and then linearize our test about this point. Let $f_j(x) = (x - \mu_j)^T Q_j (x - \mu_j)$. Note that $f_j(x^*) = \Delta_j^T Q_j \Delta_j = (k_j^*)^2$. We can immediately see that point $x_0 = \mu_j + \frac{1+\epsilon}{k_j^*} \Delta_j$ will be outside of the ellipsoid for any $\epsilon > 0$ since $f_j(x_0) = (x_0 - \mu_j)^T Q_j (x_0 - \mu_j) = \frac{(1+\epsilon)^2}{(k_j^*)^2} \Delta_j^T Q_j \Delta_j = (1+\epsilon)^2 > 1$. Note that this point x_0 lies on the ray starting from the center of the ellipsoid μ_j and passing through the center of the robot at x^* . We then linearize the constraint $f_j(x)$ about x_0 . Taking the derivative

yields $\frac{df_j}{dx}(x) = 2(x - \mu_j)^T Q_j$. The linear approximation of the constraint is then $f_j(x) \approx f_j(x_0) + \left[\frac{df_j}{dx}(x_0) \right] (x - x_0) = (1+\epsilon)^2 + 2(x_0 - \mu_j)^T Q_j (x - x_0) \geq 1$. Plugging in $x_0 = \mu_j + \frac{1+\epsilon}{k_j^*} \Delta_j$ and simplifying yields the given expression $\Delta_j^T Q_j x \geq \frac{k_j^*}{1+\epsilon} + \Delta_j^T Q_j \mu_j$.

We need to also prove that the above constraint is a supporting hyperplane by showing that all feasible points when the constraint is equality is necessarily outside of the ellipsoid parametrized by Q_j . Recall that $x_0 = \mu_j + \frac{\Delta_j}{k_j^*}$ is a point both on the surface of the ellipsoid and on the hyperplane. Therefore, all feasible points on the hyperplane can be expressed as $x = x_0 + \delta$, where $\Delta_j^T Q_j \delta = 0$. If the hyperplane supports the ellipsoid parametrized by Q_j , then necessarily $f(x) = (x - \mu_j)^T Q_j (x - \mu_j) \geq 1$. For all points on the hyperplane, the ellipsoid constraint evaluates to

$$\begin{aligned} f_j(x_0 + \delta) &= \left(\frac{1+\epsilon}{k_j^*} \Delta_j + \delta \right)^T Q_j \left(\frac{1+\epsilon}{k_j^*} \Delta_j + \delta \right) \\ &= \underbrace{\frac{(1+\epsilon)^2}{(k_j^*)^2} \Delta_j^T Q_j \Delta_j}_{=(1+\epsilon)^2} + \underbrace{\delta^T Q_j \delta}_{\geq 0} + \underbrace{\frac{2(1+\epsilon)}{k_j^*} \Delta_j^T Q_j \delta}_{=0} > 1. \end{aligned}$$

Therefore, the constraint in Proposition 2 is a supporting hyperplane. \square

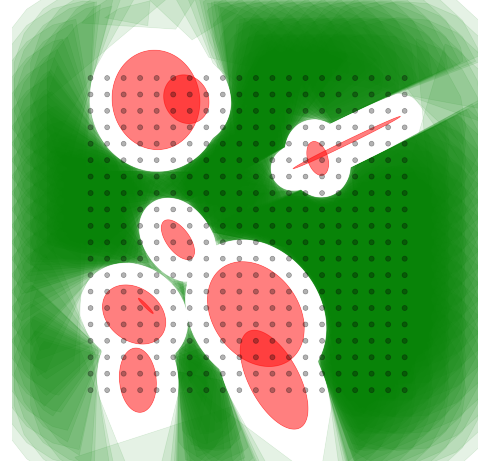


Fig. 2. Our supporting hyperplane algorithm finds safe polytopes (green) in the presence of ellipsoidal obstacles (red) regardless of the safety of the query point. We also show that our algorithm is space-filling (and therefore non-conservative) by querying points on a grid (black dots) representing a robot with some radius. The resulting union of safe polytopes converges to the full extent of the collision-less space in the limit.

Corollary 4. *Based on Corollary 1, the polytopes will also be guaranteed safe regardless of the sampling scheme used to approximate A_j . Let \hat{s} be the sampled s that maximizes $K(s)$. We then use \hat{s} to generate \hat{Q}_j and \hat{k}_j . The point \hat{x}_0 calculated using the sampled values lies on the constraint hyperplane and is farther away from the ellipsoid than the true x_0 because the sampled $\hat{k}_j \leq k_j^*$.*

This allows us to use the polytope generation with our parallelized sampling method in a safe way. We additionally note that the above constraints and polytopes apply to ellipsoidal robot bodies, as we never relied on the structure of Q_j beyond it being symmetric and positive-definite. We believe that these findings related to ellipsoid-based environment representations may have an impact beyond the scope of safety, such as in graphics.

F. Generating Paths

Our planning pipeline is amenable to sampling-based planners such as RRT and safe polytopic planners which generate safe corridors, described in the subsequent discussion.

1) *RRT*: Splat-Nav can utilize an out-of-the-box RRT solver from OMPL [40], replacing the default collision checker with a custom checker that uses our formula from Corollary 3. This checker loads in the ellipsoids generated by GSplat, initializes a KD tree using the means, and then checks for collision for any sampled point within the RRT. We evaluate this method as a baseline compared to our proposed approach which plans through safe flight corridors.

2) *Safe Flight Corridors*: Splat-Plan generates feasible motion plans using the safe flight corridor method from [27], leveraging Proposition 2 to generate safe polytopes. To do this, we create a 3D binary occupancy grid using only the means of the Gaussians.¹ We then use A* to generate a candidate path. Each point on the A* path almost always has sufficient free space in its neighborhood, and will not be stuck in corners since the path is fully connected from start to goal. However, there may be cases where the union of polytopes queried on the A* is disconnected, leading to an infeasible trajectory, which may happen when the A* path goes through walls of ellipsoids. To remedy this, we execute A* multiple times, running our collision test 3 for intersections and updating our occupancy grid accordingly. In this way, the final A* path is guaranteed to converge to a safe path. This fact, along with the fact that polytopes generated from safe points necessarily contain those points, guarantees the generation of a connected polytopic corridor. In Splat-Plan, we propose two approaches to planning:

a) *Full Trajectory*: In this approach, we first solve the planning problem for a full trajectory from the start to the goal. Using the iterated A* path, we generate a sequence of polytopes using Proposition 2. Subsequently, we find a minimal representation of the sequence of polytopes, since some constraints in the polytopes are redundant. Finally, we use the same method as Liu et al. [27] to find a smooth, dynamically feasible trajectory by solving a quadratic program. Since we are optimizing over the control points of a B-spline constrained to lie within the polytopes, we can guarantee that the paths are safe in the continuum, by the convex hull property of B-splines.

b) *Local Trajectory*: Although we find a minimal representation for the polytopes, these polytopes can still contain

many facets, and there may be many polytopes in the corridor. We note that Liu et al. [27] sparsify their point cloud to reduce the number of constraints in their problem to achieve real-time performance. Instead, we take a model predictive control (MPC) perspective, planning a trajectory over a receding time horizon and replanning before the robot reaches the end of this partial trajectory. Using the same set of polytopes (which are quick to compute) as the Full Trajectory, our MPC problem uses the current safe polytope and plans a path to the A* waypoint in the next polytope. This greatly reduces the number of constraints in the trajectory optimization problem, allowing us to achieve real-time performance. Because this one-step look-ahead method still uses the same set of polytopes as the Full Trajectory, the solved trajectories will still be guaranteed safe, at the expense of sub-optimality.

Remark 1. *An arbitrary, continuous sequence of points (e.g., a straight line from start to goal) may not generate a connected sequence of polytopes. This may occur when a particular point offers no safe polytope (i.e., a point is immediately surrounded on all sides by ellipsoids) or the sequence of points biases the polytopes into a corner so that polytopes exist on both sides of the corner, but not in the corner itself. While there may exist ways to carefully account for these edge-cases when building a trajectory, we leave this to future work.*

IV. POSE ESTIMATION

We present our pose estimation module, Splat-Loc, for localizing a robot in a Gaussian Splatting representation of its environment. We assume that the robot has an onboard RGB-D camera with known camera intrinsics. We note that prior knowledge of an estimate of the robot’s pose (such as its neighborhood) may not be available in many practical settings. As such, we design a pose estimation module that can perform global localization (i.e., pose initialization) and can utilize prior knowledge of the pose when available to speed up operation (i.e., a recursive estimation algorithm). We assume that the robot has an onboard camera with known camera intrinsics, capturing images of its environment, which we utilize in estimating the robot’s pose.

A. Global Initialization

When a good initial guess of the robot’s pose is unavailable, we execute a global pose estimation procedure. We first use the RGB-D image and the known camera intrinsics to generate the point cloud (in the camera frame). In addition, we generate a point cloud of the scene from the GSplat using the ellipsoid means $\{\mu_j\}_{j=1}^N$. This then becomes a point-cloud registration task, which we can leverage existing tool to solve. The point-cloud registration problem is given by:

$$T^* = \arg \min_{T \in \text{SE}(3)} \sum_{(p,q) \in \mathcal{C}} \|p - Tq\|_2^2, \quad (3)$$

where the transformation matrix $T \in \text{SE}(3)$ comprises of a translation component $t \in \mathbb{R}^3$ and a rotation matrix $R \in \text{SO}(3)$ and \mathcal{C} denotes the set of correspondences, associating the points between the two point clouds (where p is in

¹This may not result in a safe path, which we can handle but [27] cannot.

the map cloud and q is in the sensor cloud). Given a known set of correspondences, we can compute the optimal solution of (3) using Umeyama’s method [47].

In practice, we do not have prior knowledge of the set of correspondences \mathcal{C} between the two point clouds. To address this challenge, we apply standard techniques in feature-based global point-cloud registration. We begin by computing 33-dimensional Fast Point Feature Histograms (FPFH) descriptors [38] for each point in the point-cloud, encoding the local geometric properties of each point. Prior work has shown that visual attributes can play an important role in improving the convergence speed of point-cloud registration algorithms [34], something that FPFH does not do. To solve this, we augment the FPFH feature descriptor of a given point with its RGB color. We then identify putative sets of correspondences using a nearest-neighbor query based on the augmented FPFH descriptors then utilize Random Sample Consensus (RANSAC) to iteratively remove identify outliers to get the final \mathcal{C} . The RANSAC convergence criterion is based on the distance between the aligned point clouds and the length of a pair of edges defined by the set of correspondences.

Remark 2. *We assume the ellipsoids in \mathcal{G} are small enough (in a relative sense) such that the collection of Gaussians can be approximated by a point cloud. This assumption is automatically valid when camera viewpoints are far enough away from the scene that the point cloud projected onto the image plane is not sparse. Even if this is not the case, there are two ways in which sparsity can come into play: Gaussian-to-point sparsity and representation sparsity. If there exists large Gaussians in the scene or field of view, these can be subdivided into smaller children Gaussians without any degradation of quality to the representation. This is identical to sampling large Gaussians to add to the point cloud instead of simply taking the center. If there are no Gaussians in a particular area, trying to draw any results like a pose estimate is ill-posed because the representation lacks any information there.*

B. Recursive Pose Estimation

The recursive pose estimators initializes itself from either a known initial pose or the the global estimate. It then allows the robot to efficiently track its pose as it moves. Our recursive pose estimator requires only an RGB image (no depth).

We first render a set of 2D images of the GSplat map within a local neighborhood of the previously known pose. We then identify keypoints and the associated descriptors for points in these map images as well as the robot’s RGB image using the encoder-decoder-based method SuperPoint [6]. Next, we match features between both images using the transformer-based method LightGlue [26].² We again utilize RANSAC to remove outliers from the set of matched features to yield the final correspondence set \mathcal{C} . Finally, we take the map points from \mathcal{C} and project them into the 3D scene using

²Other methods for feature detection and matching can be utilized, such as Scale-Invariant Feature Transform (SIFT) [5] and Oriented FAST and Rotated BRIEF (ORB) [37].

the perspective projection model, camera intrinsics, and the rendered depth from GSplat.

We can then estimate the pose of the robot using the Perspective- n -Point (PnP) problem, given by:

$$T^* = \arg \min_{T \in \text{SE}(3)} \sum_{(p,w) \in \mathcal{C}} d(\Pi(T, p), w), \quad (4)$$

where $T \in \text{SE}(3)$ denotes the camera extrinsic parameters, \mathcal{C} denotes the set of correspondences between points in the environment p and points in the observed RGB image w , $\Pi : \mathbb{R}^3 \rightarrow \mathbb{R}^2$ represents the perspective projection model of point p using camera extrinsics T , and $d : \mathbb{R}^2 \times \mathbb{R}^2 \rightarrow \mathbb{R}$ denotes the reprojection error. One common choice for d is the ℓ_2 -squared-norm, which we also utilize in this work. This yields a non-linear least-squares optimization problem that can be solved using variants of the Levenberg-Marquardt and Gauss-Newton optimization algorithms. We note that various methods have been developed to solve the PnP problem such as the EPnP [25], DLS [14], and SQPnP [44] methods.

Remark 3. *In many robotics problems, an estimate of the covariance associated with the estimated pose of the robot is important for downstream decision-making and motion planning. In this work, we compute the Hessian of (4) at T^* to estimate the covariance associated with the estimated pose of the robot.*

Remark 4. *Our method can be directly extended to the batch-estimation case where we solve a bundle adjustment problem over multiple time steps.*

V. RESULTS

We examine the performance of each component of our navigation and pose estimation pipeline and perform ablative studies, comparing our algorithms to existing methods. We evaluate our proposed pose estimator in one synthetic scene **Stonehenge** and two real scenes (trained from real RGB images) **Statues** and **Flightroom**, shown in Fig. 3.

A. Safe Planning

We evaluate Splat-Plan, our polytopic safe corridor method, on 100 start and goal locations distributed across a circle in the three environments. We also compare it against baselines and prior work. Namely, we benchmark against: (1) an A* planner using the GSplat means as an occupancy grid, (2) an RRT* planner using the collision test 3, and (3) a gradient-based planner built for neural-network NeRFs, Nerf-Nav [1].

We also present several ablations and extensions of Splat-Plan. First, we investigate the properties of a more probabilistically grounded perspective on the ellipsoidal GSplat representation. Specifically, we compare using just the ellipsoid represented by the GSplat covariances (Splat-Plan Basic) to scaling the ellipsoids by a factor $\beta_j \alpha_j$, where β_j is related to the confidence interval of the Gaussian and α_j is the opacity of the Gaussian. This scaling therefore represents the joint probability of an object existing in an ellipsoidal region of

space and that of the object being solid. For these experiments, we take $\beta_j = 2$.

We also benchmark our claims between the Full Trajectory and Local Trajectory methods (Iterative A* following), an ablation of Full Trajectory that does not iterate on A* (Non-iterative A*), and a Local Trajectory method that naively uses a straight line path to the goal to create polytopes instead of A*. Then present hardware experiments onboard a drone in the **Flightroom** environment. For all tests, we parametrize the robot body as a sphere with radius $r = 0.03$, except for the hardware tests, where $r = 0.28$ m.

Visually, the paths generated by Splat-Plan are smooth, safe, and non-conservative (Fig. 3). This fact is validated in Fig. 4, where Splat-Plan’s trajectories (probabilistic and basic variants) are safe (distances greater than 0) with respect to the *ground-truth mesh* in a vast majority of trials. Moreover, these trajectories are non-conservative due to small path lengths and variances. We also see that the probabilistic variant is slightly safer and has marginally smaller path lengths. Using the GSplat means and a gradient-based planner has no performance guarantees and therefore suffer in safety. The RRT* also suffers due to tradeoff between resolution of the collision checking and the lack of scalability in sampling random points.

Although the Full Trajectory method presented in Fig. 4 is generalizable, we wanted to test the limits of the safe corridor generation by benchmarking the Local Trajectory method and removing components of the Full Trajectory. We see that all methods are safe (Fig. 5) due to the robust guarantees of Proposition 2. The Local Trajectory method (Iterative A* Following) always succeeds in finding feasible trajectories to the goal, validating our performance claim. The sub-optimality of the path lengths are also apparent. Without relying on the iterative A* procedure (Non-Iterative A*), the feasibility and connectivity of trajectories falls to 55% due to the “corner” phenomenon (Remark 1). Interestingly, removing A* entirely and sampling corridor query points on the line between the current and goal location (Line Following) is surprisingly performant, able to navigate to the goal 58% of the time. Finally, we executed Splat-Plan (probabilistic variant) on the real Flightroom environment onboard a drone ($r = 0.28$ cm). Visually and qualitatively, the executed trajectory is safe, which we demonstrate in Figure 6.

B. Pose Estimation

We compare our proposed pose estimator to other pose estimation methods, including Point-to-plane Iterative Closest Point (ICP) [4] and Colored-ICP [34]. In addition, we examine two variants of our pose estimator: Splat-Loc-GLue, which utilizes LightGlue for feature matching; and Splat-Loc-SIFT, which utilizes SIFT for feature matching. In each scene, we run 10 trials (of 100 frames each) of each pose estimation algorithm. We evaluate the rotation and translation errors with respect to the ground-truth pose as well as the computation time per frame and the success rate (a success means it generated a solution, regardless of quality).

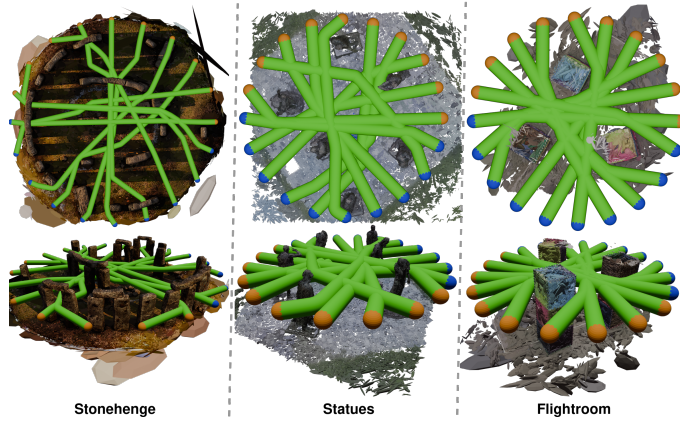


Fig. 3. Qualitative results of 10 safe trajectories using our proposed method with start (orange) and goal (blue) states spread over a circle. The widths of the trajectories are the same size as the robot body. We see that the trajectories are safe, but not conservative.

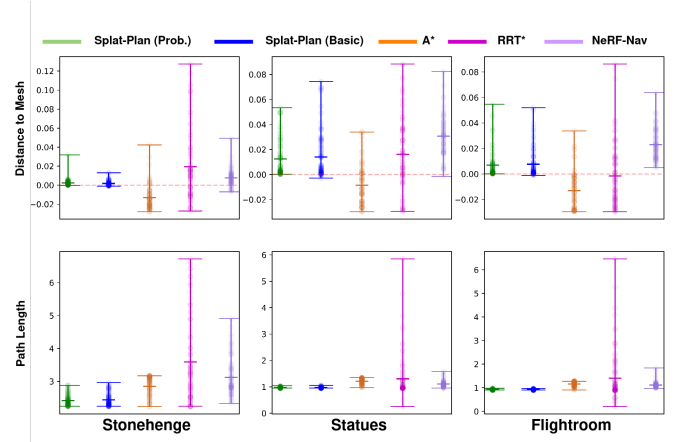


Fig. 4. A comparison of trajectories generated by our method and 3 other baselines (A*, RRT*, and NeRF-Nav [1]) for the same 100 start and end locations for each scene (Stonehenge, Statues, and Flightroom). We evaluate the safety and conservativeness of trajectories based on distance to the scene mesh and the length of the path, respectively. Each dot represents a particular trajectory’s minimum distance to the mesh and its path length, and horizontal markings indicate the max, mean, and min over all trajectories. By using a probabilistic weighting on the scaling of the ellipsoids in the representation, our proposed method is able to be safe (min. distance greater than 0) and is not conservative (small path length and variance).

The performance of pose estimation algorithms often depends on the error associated with initial estimate of the pose. As such, we seek to examine these algorithms across settings with different errors in the initial estimate of the pose. In this study, we do not utilize the initialization procedure described in Section IV, rather we assume an initial estimate of the pose is available. We generate the initial estimate by taking the ground truth pose then applying a rotation δ_R about a random axis and the translation δ_t in a random direction.

1) *1) Pose Initialization of Splat-Loc:* We evaluate the global point-cloud alignment initialization procedure as well as the

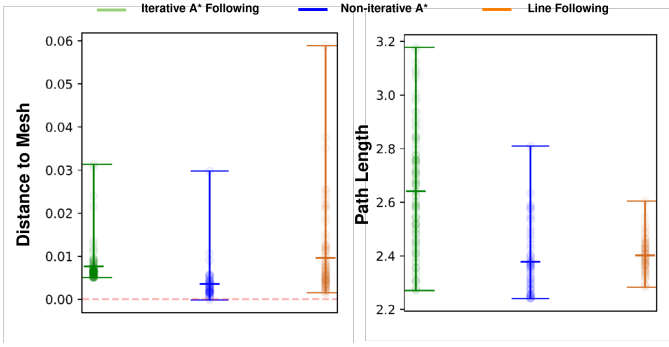


Fig. 5. Extensions and ablations of Splat-Plan evaluated on the same configurations as Figure 4 on Stonehenge. We compare three methods: iterative A* following, non-iterative A* following, and line following. All the methods are still safe (distances greater than 0) because they use polytopic corridors. Iterative A* has a 100% success rate by nature of the interaction between the safe polytopes and a guaranteed safe A* path. Non-iterative A* could not find a solution 45% of the time due to the inability to find a connected union of polytopes generated by the A*. Finally, line following produced infeasible programs 18% of the time, and timed out getting to the goal (i.e. "stuck") 24% of the time.

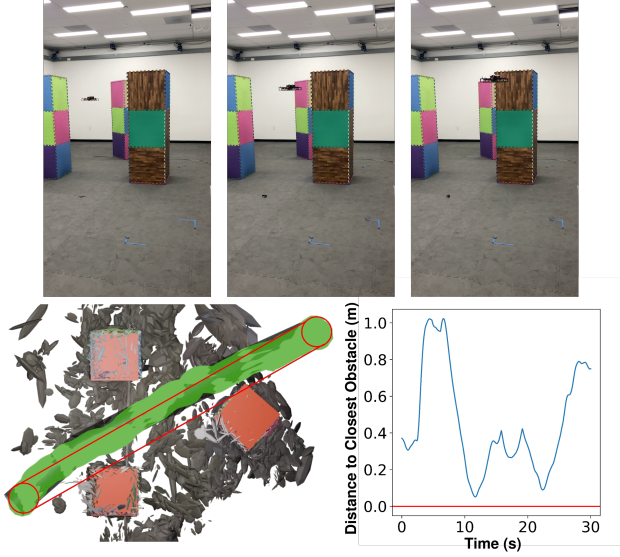


Fig. 6. (top) Deployment of our safe planner, Splat-Plan, on a drone. (bottom-left) Visualization of the executed trajectory (green) and the commanded trajectory (black outline). A straight line path from start to goal is not safe. (bottom-right) Distance of the drone to the closest obstacle, taking into account the extent of the drone. Note that the executed trajectory lies above the red line and is therefore safe.

performance of Splat-Loc-Glue in the Statues scene (a real-world scene) and Stonehenge (a synthetic scene), with the results in Table I. We see that the success rate is 80% in both scenes and it runs at approximately 20-30 Hz. When it does succeed, the pose errors are on the order of 0.3 deg and 1 cm. Although these estimates are relatively good, we note that these are less accurate than the recursive pose estimates discussed later.

2) *Recursive Pose Estimation*: Table II shows our performance metrics in the Statues scene with $\delta_R = 20^\circ$ and $\delta_t = 0.1$ m. First, we see that only the Colored-ICP algorithm fails to achieve a 100% success rate. Second, our algorithms Splat-Loc-Glue and Splat-Loc-SIFT yield higher-accuracy and more consistent solutions, with mean rotation and translation errors less than 0.1 deg and 7 mm, respectively, and lower standard deviations. In these tests, Splat-Loc-Glue performs the best on each metric with a computation time of about 35 ms. Figure 7 shows a run of the algorithms where ICP and Colored-ICP achieve relatively lower errors.

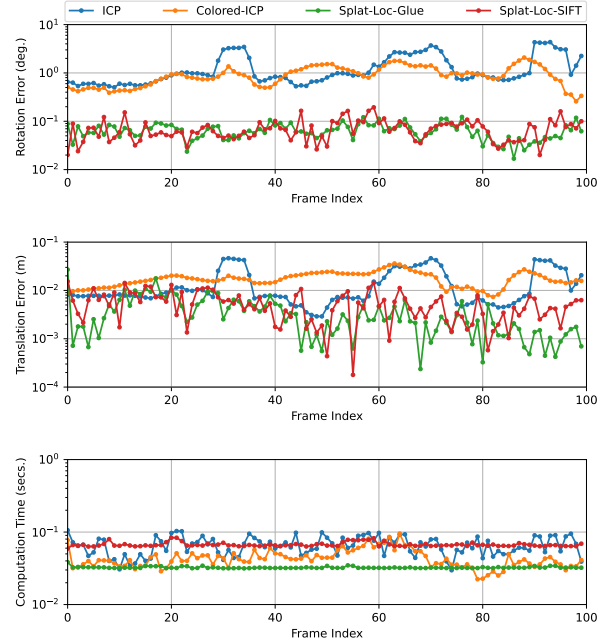


Fig. 7. **Statues** Scene with $\delta_R = 20^\circ$ and $\delta_t = 0.1$ m—Pose error and computation time per frame achieved by each pose estimation algorithm in a specific instance of the problem where ICP and Colored-ICP perform well.

Next, Table III shows results for the **Statues** scene with $\delta_R = 30^\circ$ and $\delta_t = 0.5$ m. Note that the success rates of Colored-ICP and Splat-Loc-SIFT decreases sharply, suggesting that these methods require a good initial estimate of the pose of the robot. However, when they do succeed, these algorithms achieve low rotation and translation errors, with Splat-Loc-SIFT achieving a much-higher accuracy compared to Colored-ICP. In contrast, the Splat-Loc-Glue algorithm achieves a perfect success rate, along with the lowest rotation and translation errors and computation time. The results suggest the greater robustness of Splat-Loc-Glue compared to Splat-Loc-SIFT. Figure 8 shows the performance of each algorithm in an instance of the problem where all methods are successful.

We present additional results on the **Flightroom** scene in the Appendix.

TABLE I
PERFORMANCE OF THE POSE INITIALIZATION MODULE IN SPLAT-LOC

Scene	Rotation (deg.)	Translation Error (m)	Computation Time (secs.)	Success Rate (%)
Statues	$3.683e^{-1} \pm 7.207e^{-1}$	$1.332e^{-2} \pm 2.329e^{-2}$	$3.387e^{-2} \pm 5.696e^{-4}$	80
Stonehenge	$2.138e^{-1} \pm 2.068e^{-1}$	$3.026e^{-3} \pm 2.274e^{-3}$	$4.572e^{-2} \pm 1.697e^{-3}$	80

TABLE II
COMPARISON OF POSE ESTIMATION ALGORITHMS IN THE STATUES SCENE WITH $\delta_R = 20^\circ$ AND $\delta_t = 0.1$ m

Algorithm	Rotation (deg.)	Translation Error (m)	Computation Time (secs.)	Success Rate (%)
ICP [4]	$8.416e^1 \pm 5.578e^1$	$3.829e^0 \pm 8.507e^0$	$8.595e^{-2} \pm 4.398e^{-2}$	100
Colored-ICP [34]	$3.020e^1 \pm 4.573e^1$	$3.455e^{-1} \pm 5.102e^{-1}$	$6.270e^{-2} \pm 2.716e^{-2}$	80
Splat-Loc-SIFT (ours)	$8.314e^{-2} \pm 9.367e^{-3}$	$5.720e^{-3} \pm 7.619e^{-4}$	$6.557e^{-2} \pm 7.158e^{-4}$	100
Splat-Loc-Glue (ours)	$5.726e^{-2} \pm 4.815e^{-3}$	$3.129e^{-3} \pm 3.232e^{-4}$	$3.412e^{-2} \pm 1.992e^{-3}$	100

TABLE III
COMPARISON OF POSE ESTIMATION ALGORITHMS IN THE STATUES SCENE WITH $\delta_R = 30^\circ$ AND $\delta_t = 0.5$ m

Algorithm	Rotation (deg.)	Translation Error (m)	Computation Time (secs.)	Success Rate (%)
ICP [4]	$9.897e^1 \pm 3.051e^1$	$1.401e^0 \pm 2.297e^{-1}$	$4.354e^{-2} \pm 5.071e^{-2}$	100
Colored-ICP [34]	$2.419e^0 \pm 1.609e^0$	$2.183e^{-1} \pm 2.016e^{-1}$	$7.029e^{-2} \pm 2.435e^{-2}$	20
Splat-Loc-SIFT (ours)	$7.844e^{-2} \pm 5.953e^{-3}$	$6.275e^{-3} \pm 8.400e^{-4}$	$7.312e^{-2} \pm 1.498e^{-3}$	30
Splat-Loc-Glue (ours)	$6.139e^{-2} \pm 5.994e^{-3}$	$3.671e^{-3} \pm 6.535e^{-4}$	$4.278e^{-2} \pm 1.498e^{-3}$	100

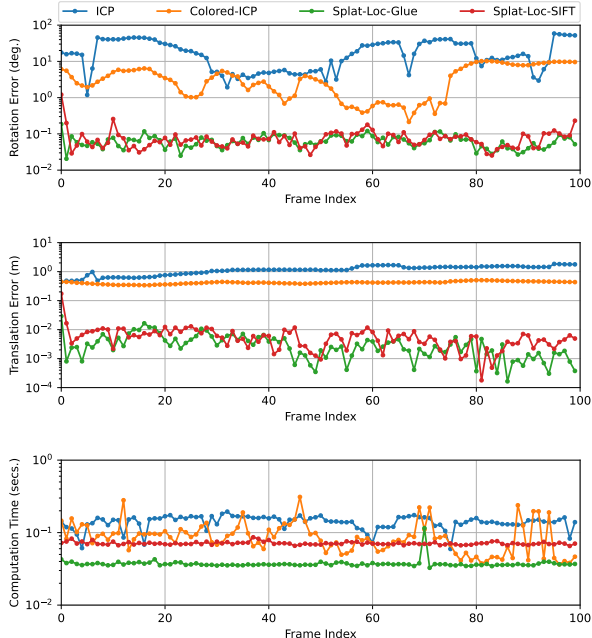


Fig. 8. **Statues** Scene with $\delta_R = 30^\circ$ and $\delta_t = 0.5$ m—Pose error and computation time per frame achieved by each pose estimation algorithm in an instance where Colored-ICP and Splat-Loc-SIFT are successful.

VI. CONCLUSION

We introduce an efficient navigation pipeline termed *Splat-Nav* for robots operating in Gaussian Splatting envi-

ronments. *Splat-Nav* consists of a guaranteed-safe planning module *Splat-Plan*, which allows for real-time planning (5 Hz) by leveraging the ellipsoidal representation inherent in GSplats for efficient collision-checking and safe corridor generation, facilitating real-time online replanning. Moreover, our proposed pose estimation module *Splat-Loc* computes high-accuracy pose estimates faster (20 Hz) and more reliably compared to existing pose estimation algorithms for radiance fields, such as NeRFs. We present extensive simulation results, highlighting the effectiveness of *Splat-Nav*. In future work, we seek to more deeply explore utilization of *Splat-Nav* across a diversity of hardware platforms and real-life environments.

APPENDIX

A. Planning Computation Times

In addition to outperforming other existing methods in safety and path length of computed paths (Fig. 4,5), our *Splat-Plan* method achieves faster computation times compared to the point-based motion planners RRT* and NeRF-Nav; generates smooth trajectories unlike the RRT*, NeRF-Nav, and A*; and detects infeasible planning problems. We remind the reader of the following baselines: RRT*, A*, and polytopic A*. RRT* (implemented in OMPL) replaces the default collision checker with our ellipsoid-to-ellipsoid collision test in Proposition 1. The A* methods use the means of the Gaussians in GSplat to create a binary occupancy grid. A* simply plans a shortest path through the binary grid. Polytopic A* goes one step further, constructing safe polytopes through Proposition 2 on the A* waypoints, from which it computes a B-spline trajectory passing through all the polytopes. *Splat-Plan* is a

further refinement of the Polytopic A* algorithm. Instead of a single instance of A*, we iterate between querying A* and updating the binary occupancy grid at the A* waypoints that are unsafe via the collision test in Proposition 1. Typically, the Splat-Plan method requires only a handful of A* iterations (< 5), and the generation of polytopes for approximately 100 A* waypoints runs at approximately 100 Hz.

Splat-Plan is much faster than RRT* and NeRF-Nav [1] due to our method's inherent sampling efficiency, as noted in Table IV. The faster computation time in Splat-Plan results primarily from the fast safe polytope generation procedure. Because both of these baselines also test/measure safety point-wise, they have finite resolution. Therefore, these baselines may not dynamically feasible for some robotic tasks, and may be unsafe in certain regions of the computed trajectory, if the resolution is insufficient.

The creation of polytopes also endows our method with the ability to fail gracefully. A smooth curve can be created from the start to goal locations so long as a connected series of safe polytopes are given. Since the polytopes generated are inherently safe, we can simply check for overlap between consecutive pairs of polytopes. In this work, for simplicity, we choose to solve an LP to determine overlap. Typically, this operation can be performed at more than 10 Hz for the entire trajectory. Of course, less computationally-intensive methods exist, such as the GJK algorithm to determine collision between convex objects. Using the connectivity of polytopes as a failure signal, we observe that by not updating the occupancy grid and subsequently executing A*, polytopic A* can only achieve feasible safe trajectories 55% out of 100 configurations. This is due to the corner phenomenon in Remark 1, where safe polytopes existing on both sides of an ellipsoidal wall are disconnected.

Since Splat-Plan requires the use of A* to initialize a path to generate the safety polytope corridors, it will necessarily be slower than these A* baselines. However, we note that in the Full Trajectory regime, the dominating cost is the calculation of the B-spline due to the number of polytopes in the constraints, with many facets per polytope. This QP was solved using CVXPY with the Clarabel solver. We note that the computation time associated with the B-spline computation procedure can be reduced using embedded solvers or faster programming languages.

TABLE IV
COMPARISON OF FULL TRAJECTORY PLANNING ALGORITHM COMPUTATION TIMES.

Algorithm	Times (s)	Smooth	Failure Signal
NeRF-Nav [1]	2.325	✗	✗
RRT*	9.489 ± 5.128	✗	✗
A*	0.0508 ± 0.00956	✗	✗
Non-iterative, Polytopic A*	0.1222 ± 0.03636	✓	✓(55%)
Splat-Plan (ours)	0.892 ± 0.2896	✓	✓(100%)

Since the polytope and A* computation procedures are relatively fast, while computation of the B-spline is relatively slow, we can compute the B-spline for some small time step in

the future, in a receding-horizon manner. In our experiments, this amounted to fitting a B-spline through the current and next polytope. Since the Full Trajectory method finds a connected series of polytopes and is therefore always able to fit a B-spline connecting the start position to goal position, the Local Trajectory method can also still guarantee safety and feasibility since the entire constraint set is separable based on time, at the expense of the optimality of the solution.

We found the 55% success rate of the polytopic A* to be surprisingly high, which speaks to the ability of our polytopes to be generated even when query points are unsafe. To push the limits of generalizability of the polytopes, we implemented a simple line following planner based on the polytopes. Specifically, in this baseline, we query a polytope at the robot's current position, and another polytope at a point some small distance away (0.02 in our evaluations) on the line between the current position and the goal position, then solve for a B-spline. Such a method did not yield connected polytopes for 18% of configurations, and got stuck (ran for over 200 iterations) for 24% of configurations. Note that while the robot was stuck, the B-spline was still guaranteed safe (Fig. 5).

TABLE V
COMPARISON OF LOCAL TRAJECTORY PLANNING ALGORITHM COMPUTATION TIMES.

Algorithm	Times (s)	Smooth	Failure Signal
Line Following	0.01492 ± 0.00858	✓	✓(58%)
Splat-Nav (ours)	0.15241 ± 0.07588	✓	✓(100%)

B. Pose Estimation: Comparison to Gradient-Based Pose Estimators

We compare the performance of the pose estimation algorithms in this work to a gradient-based pose estimator amenable to Gaussian Splatting, termed iNeRF-GS, similar to iNeRF [52], a canonical pose estimator amenable to NeRFs. We note that publicly-available codebases for Gaussian Splatting do not provide analytical gradients required for gradient-based pose estimation. In addition, Gaussian Splatting does not support automatic differentiation. As a result, we leverage finite differences to estimate the gradient of the photometric loss function utilized in the pose estimator (please refer to [52] for additional details on gradient-based pose estimation in radiance fields). We note that our implementation might not be particularly fast, given the approach utilized in estimating the gradients. We provide the summary statistics of the error in the pose estimates computed by each algorithm, in addition to the computation time on a trial with 100 frames in the Statues scene in Table VI. We note that all methods had a perfect success rate in this problem. The iNeRF-GS algorithm achieves the lowest accuracy and requires the greatest computation time, unlike Colored-ICP, Splat-Loc-SIFT, and Splat-Loc-Glue, which achieve much-higher accuracy with a rotation error less than a degree and a translation error less than 15cm. iNeRF-GS requires a computation time of about

36.15 secs per frame, which is about two orders of magnitude slower than the next-slowest method ICP, which requires a computation time of about 110 milliseconds. Colored-ICP, Splat-Loc-SIFT, and Splat-Loc-Glue require less than 100 milliseconds of computation time. Compared to all methods, Splat-Loc-Glue yields pose estimates with the lowest mean rotation and translation error, less than 0.06 deg. and 4mm, respectively, and achieves the fastest mean computation time, less than 42 milliseconds.

C. Recursive Pose Estimation

Table VII presents the results in the **Flightroom** scene with $\delta_R = 50^\circ$ and $\delta_t = 0.2$ m. We note that the Gaussian Splatting representation of the Flightroom scene was of much lower quality, which negatively impacted the performance of many of the pose estimation algorithms. As a result, we attempt to mitigate its impact by ensuring that the robot captures informative images during the duration of the problem. ICP and Colored-ICP always succeed but yield pose estimates of notably low accuracy, with mean rotation errors of about 120 deg and 125 deg and translation errors of about 11.59 m and 0.73 m, respectively. In contrast, Splat-Loc-SIFT fails to produce an estimate in all trials. However, Splat-Loc-Glue achieves a perfect success rate, yields high-accuracy pose estimates with a mean rotation error of about 0.3 deg and a mean translation error less than 5 mm, and takes an average of 37.74 ms per frame. Figure 9 shows the errors in the pose estimates for a single trial.

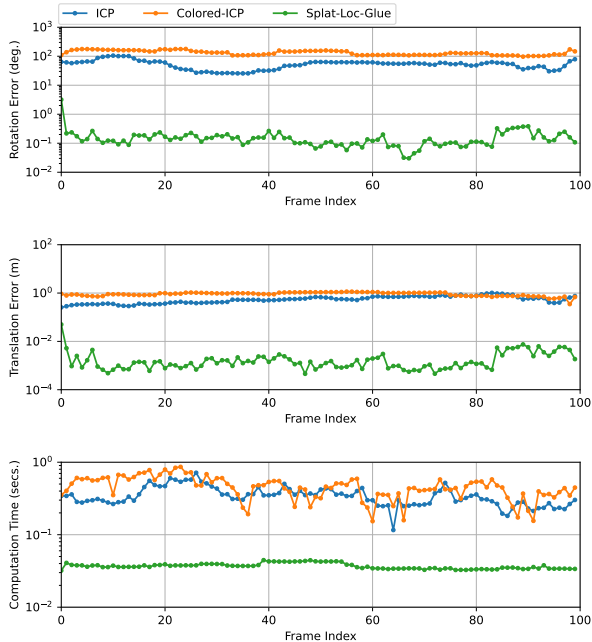


Fig. 9. **Flightroom** Scene with $\delta_R = 50^\circ$ and $\delta_t = 0.2$ m—Pose error and computation time per frame achieved by each pose estimation algorithm. Splat-Loc-SIFT was not successful on any trial and is thus omitted in the figure. While ICP and Colored-ICP fail to provide accurate estimates of the robot’s pose, Splat-Loc-Glue computes high-accuracy pose estimates.

Here, we examine the performance of each pose estimation algorithm in a synthetic scene **Stonehenge**, beginning with initial rotation and translation errors of 20 deg. and 0.1m. Table VIII shows the performance of each algorithm across the ten trials. Similar to the results observed with the real-world scene, Splat-Loc-SIFT and Splat-Loc-Glue yield high-accuracy pose estimates with average rotation and translation errors less than 0.5 deg and 5mm respectively, unlike the ICP and Colored-ICP which produce low-accuracy estimates. Moreover, ICP and Colored-ICP seem to diverge in some runs as the estimation procedure proceeds over time, depicted in Figure 10. In contrast, Splat-Loc-Glue achieves a perfect success rate, in contrast with Splat-Loc-SIFT, which achieves a 90% success rate, in addition to attaining the fastest computation time.

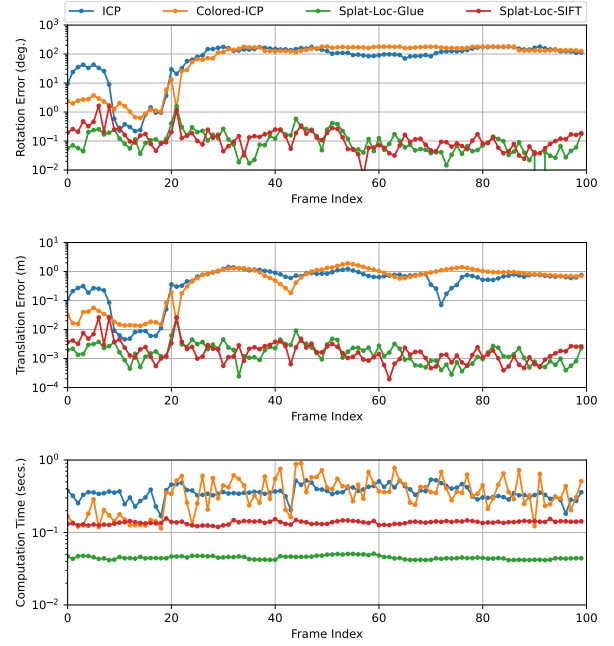


Fig. 10. **Stonehenge** Scene with $\delta_R = 20^\circ$ and $\delta_t = 0.1$ m—While ICP and Colored-ICP diverge over time, Splat-Loc-SIFT and Splat-Loc-Glue do not diverge, producing high-accuracy estimates.

In addition, we examine the performance of the pose estimation algorithms in problems with a larger error in the initial estimate of the pose, with $\delta_R = 30^\circ$ and $\delta_t = 0.5$ m. We present the performance of each algorithm on each metric in Table IX, where we note that ICP and Colored-ICP do not provide accurate estimate of the robot’s pose. Moreover, the pose estimation errors achieved by ICP and Colored-ICP have a significant variance. In contrast, Splat-Loc-SIFT and Splat-Loc-Glue yield pose estimates of high accuracy with average rotation and translation errors less than 0.5 deg. and 5mm, respectively, similar to the setting with low errors in the initial pose estimate. However, Splat-Loc-SIFT achieves a lower success rate, compared to Splat-Loc-Glue, which achieves a perfect success rate. In Figure 11, we show

TABLE VI

COMPARISON OF POSE ESTIMATION ALGORITHMS IN THE **STATUES** SCENE WITH $\delta_R = 20^\circ$ AND $\delta_t = 0.1$ m. ALL METHODS WERE SUCCESSFUL IN THIS PROBLEM.

Algorithm	Rotation (deg.)	Translation Error (m)	Computation Time (secs.)
ICP [4]	$7.306e^1 \pm 4.584e^1$	$1.285e^0 \pm 7.496e^{-1}$	$1.064e^{-1} \pm 1.918e^{-2}$
Colored-ICP [34]	$8.272e^{-1} \pm 3.718e^{-1}$	$1.305e^{-2} \pm 5.973e^{-3}$	$4.328e^{-2} \pm 9.697e^{-3}$
Splat-Loc-SIFT (ours)	$8.590e^{-2} \pm 6.050e^{-2}$	$5.590e^{-3} \pm 7.441e^{-3}$	$6.327e^{-2} \pm 2.384e^{-3}$
Splat-Loc-Glue (ours)	$5.036e^{-2} \pm 3.088e^{-2}$	$3.298e^{-3} \pm 2.692e^{-3}$	$4.119e^{-2} \pm 7.319e^{-2}$
iNeRF-GS	$1.217e^2 \pm 3.371e^1$	$2.444e^0 \pm 9.116e^{-1}$	$3.615e^1 \pm 5.436e^0$

TABLE VII

COMPARISON OF POSE ESTIMATION ALGORITHMS IN THE **FLIGHTROOM** SCENE WITH $\delta_R = 50^\circ$ AND $\delta_t = 0.2$ m

Algorithm	Rotation (deg.)	Translation Error (m)	Computation Time (secs.)	Success Rate (%)
ICP [4]	$1.212e^2 \pm 2.957e^1$	$1.159e^1 \pm 2.601e^1$	$1.451e^{-1} \pm 1.471e^{-1}$	100
Colored-ICP [34]	$1.253e^2 \pm 3.188e^1$	$7.354e^{-1} \pm 2.540e^{-1}$	$4.847e^{-1} \pm 5.472e^{-2}$	100
Splat-Loc-SIFT (ours)	—	—	—	0
Splat-Loc-Glue (ours)	$2.539e^{-1} \pm 1.543e^{-1}$	$3.810e^{-3} \pm 2.618e^{-3}$	$3.774e^{-2} \pm 8.522e^{-4}$	100

TABLE VIII

COMPARISON OF POSE ESTIMATION ALGORITHMS IN THE **STONEHENGE** SCENE WITH $\delta_R = 20^\circ$ AND $\delta_t = 0.1$ m.

Algorithm	Rotation (deg.)	Translation Error (m)	Computation Time (secs.)	Success Rate (%)
ICP [4]	$9.702e^1 \pm 3.006e^1$	$1.085e^0 \pm 7.958e^{-1}$	$3.604e^{-1} \pm 5.036e^{-2}$	100
Colored-ICP [34]	$7.185e^1 \pm 3.224e^1$	$5.175e^{-1} \pm 2.162e^{-1}$	$3.678e^{-1} \pm 6.378e^{-2}$	100
Splat-Loc-SIFT (ours)	$1.962e^{-1} \pm 2.690e^{-2}$	$3.033e^{-3} \pm 4.268e^{-4}$	$1.399e^{-1} \pm 5.727e^{-3}$	90
Splat-Loc-Glue (ours)	$2.114e^{-1} \pm 2.265e^{-1}$	$2.962e^{-3} \pm 2.420e^{-3}$	$4.554e^{-2} \pm 1.119e^{-3}$	100

the estimation errors for a single run, highlighting the high variance in the errors associated with the pose estimates computed Colored-ICP. ICP fails to yield a pose estimate of relatively high accuracy for the duration of the problem.

REFERENCES

- [1] Michal Adamkiewicz, Timothy Chen, Adam Caccavale, Rachel Gardner, Preston Culbertson, Jeannette Bohg, and Mac Schwager. Vision-only robot navigation in a neural radiance world. *IEEE Robotics and Automation Letters (RA-L)*, 7(2):4606–4613, 2022.
- [2] Joydeep Biswas and Manuela Veloso. Depth camera based indoor mobile robot localization and navigation. In *2012 IEEE International Conference on Robotics and Automation*, pages 1697–1702. IEEE, 2012.
- [3] Timothy Chen, Preston Culbertson, and Mac Schwager. Catnips: Collision avoidance through neural implicit probabilistic scenes. *arXiv preprint arXiv:2302.12931*, 2023.
- [4] Yang Chen and Gérard Medioni. Object modelling by registration of multiple range images. *Image and vision computing*, 10(3):145–155, 1992.
- [5] Lowe David. Distinctive image features from scale-invariant keypoints. *International journal of computer vision*, 60:91–110, 2004.
- [6] Daniel DeTone, Tomasz Malisiewicz, and Andrew Rabinovich. Superpoint: Self-supervised interest point detection and description. In *Proceedings of the IEEE conference on computer vision and pattern recognition workshops*, pages 224–236, 2018.
- [7] Herbert Edelsbrunner. Surface Reconstruction by Wrapping Finite Sets in Space. In Boris Aronov, Saugata Basu, János Pach, and Micha Sharir, editors, *Discrete and Computational Geometry: The Goodman-Pollack Festschrift*, Algorithms and Combinatorics, pages 379–404. Springer, Berlin, Heidelberg, 2003. ISBN 978-3-642-55566-4.
- [8] A. Elfes. Using occupancy grids for mobile robot perception and navigation. *Computer*, 22(6):46–57, June 1989. ISSN 1558-0814.
- [9] Alhamdi Eman and Hedjar Ramdane. Mobile robot localization using extended kalman filter. In *2020 3rd International Conference on Computer Applications & Information Security (ICCAIS)*, pages 1–5. IEEE, 2020.
- [10] Dieter Fox, Sebastian Thrun, Wolfram Burgard, and Frank Dellaert. Particle filters for mobile robot localization. In *Sequential Monte Carlo methods in practice*, pages 401–428. Springer, 2001.
- [11] Igor Gilitschenski and Uwe D. Hanebeck. A robust computational test for overlap of two arbitrary-dimensional ellipsoids in fault-detection of kalman filters. In *2012 15th International Conference on Information Fusion*, pages 396–401, 2012.
- [12] Leonidas J Guibas, Rajeev Motwani, and Prabhakar

TABLE IX
COMPARISON OF POSE ESTIMATION ALGORITHMS IN THE STONEHENGE SCENE WITH $\delta_R = 30^\circ$ AND $\delta_t = 0.5$ m.

Algorithm	Rotation (deg.)	Translation Error (m)	Computation Time (secs.)	Success Rate (%)
ICP [4]	$1.303e^2 \pm 2.254e^1$	$3.697e^0 \pm 5.533e^0$	$1.217e^{-1} \pm 1.527e^{-1}$	100
Colored-ICP [34]	$9.489e^1 \pm 5.128e^1$	$5.737e^{-1} \pm 2.880e^{-1}$	$4.879e^{-1} \pm 1.038e^{-1}$	20
Splat-Loc-SIFT (ours)	$2.164e^{-1} \pm 3.682e^{-2}$	$3.335e^{-3} \pm 5.628e^{-4}$	$1.384e^{-1} \pm 3.145e^{-3}$	70
Splat-Loc-Glue (ours)	$2.193e^{-1} \pm 2.024e^{-1}$	$3.141e^{-3} \pm 2.099e^{-3}$	$4.507e^{-2} \pm 6.105e^{-4}$	100

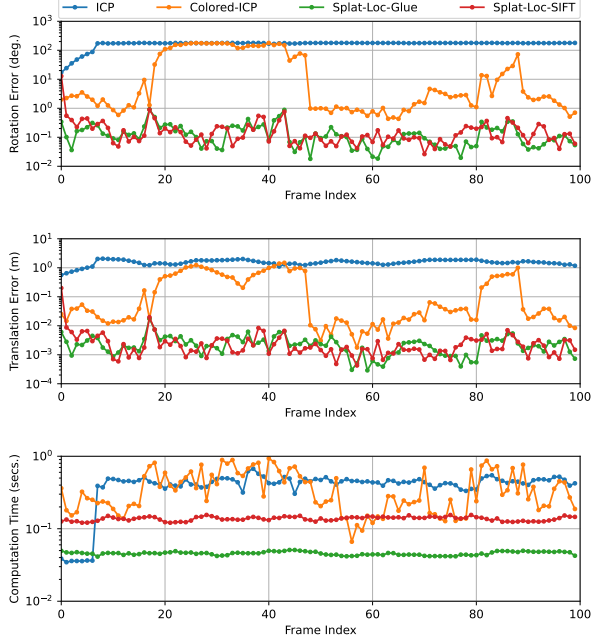


Fig. 11. Stonehenge Scenewith $\delta_R = 30^\circ$ and $\delta_t = 0.5$ m—Splat-Loc-SIFT and Splat-Loc-Glue produce pose estimates of the highest accuracy, compared to ICP and Colored-ICP. Further, Splat-Loc-Glue requires the least computation time per frame.

Raghavan. The robot localization problem. *SIAM Journal on Computing*, 26(4):1120–1138, 1997.

[13] Luxin Han, Fei Gao, Boyu Zhou, and Shaojie Shen. Fiesta: Fast incremental euclidean distance fields for online motion planning of aerial robots. *IEEE/RSJ International Conference on Intelligent Robots and Systems (IROS)*, pages 4423–4430, 2019.

[14] Joel A Hesch and Stergios I Roumeliotis. A direct least-squares (dls) method for pnp. In *2011 International Conference on Computer Vision*, pages 383–390. IEEE, 2011.

[15] Nick Alger (<https://math.stackexchange.com/users/3060/nickalger>). Detect if two ellipses intersect. Mathematics Stack Exchange, 2020. URL <https://math.stackexchange.com/q/3678498>. URL: <https://math.stackexchange.com/q/3678498> (version: 2021-05-09).

[16] Rico Jonschkowski, Divyam Rastogi, and Oliver Brock.

Differentiable particle filters: End-to-end learning with algorithmic priors. *arXiv preprint arXiv:1805.11122*, 2018.

[17] Sertac Karaman, Matthew R Walter, Alejandro Perez, Emilio Frazzoli, and Seth Teller. Anytime motion planning using the rrt. In *2011 IEEE international conference on robotics and automation*, pages 1478–1483. IEEE, 2011.

[18] Peter Karkus, David Hsu, and Wee Sun Lee. Particle filter networks with application to visual localization. In *Conference on robot learning*, pages 169–178. PMLR, 2018.

[19] Lydia E Kavraki, Petr Svestka, J-C Latombe, and Mark H Overmars. Probabilistic roadmaps for path planning in high-dimensional configuration spaces. *IEEE transactions on Robotics and Automation*, 12(4):566–580, 1996.

[20] Bernhard Kerbl, Georgios Kopanas, Thomas Leimkühler, and George Drettakis. 3D Gaussian splatting for real-time radiance field rendering. *ACM Transactions on Graphics*, 42(4), July 2023. URL <https://repo-sam.inria.fr/fungraph/3d-gaussian-splatting/>.

[21] Pileun Kim, Jingdao Chen, and Yong K Cho. Slam-driven robotic mapping and registration of 3d point clouds. *Automation in Construction*, 89:38–48, 2018.

[22] SM LaValle. Planning algorithms. *Cambridge University Press google schola*, 2:3671–3678, 2006.

[23] Steven M LaValle and James J Kuffner Jr. Randomized kinodynamic planning. *The international journal of robotics research*, 20(5):378–400, 2001.

[24] Steven M LaValle, James J Kuffner Jr, BR Donald, et al. Rapidly-exploring random trees: Progress and prospects. *Algorithmic and computational robotics: new directions*, 5:293–308, 2001.

[25] Vincent Lepetit, Francesc Moreno-Noguer, and P Fua. Epnp: Efficient perspective-n-point camera pose estimation. *Int. J. Comput. Vis.*, 81(2):155–166, 2009.

[26] P Lindenberger, PE Sarlin, and M Pollefeys. Lightglue: Local feature matching at light speed. arxiv 2023. *arXiv preprint arXiv:2306.13643*, 2023.

[27] Sikang Liu, Michael Watterson, Kartik Mohta, Ke Sun, Subhrajit Bhattacharya, Camillo J. Taylor, and Vijay Kumar. Planning dynamically feasible trajectories for quadrotors using safe flight corridors in 3D complex environments. *IEEE Robotics and Automation Letters (RA-L)*, 2(3):1688–1695, 2017. doi: 10.1109/LRA.2017.2663526.

[28] Dominic Maggio, Marcus Abate, Jingnan Shi, Courtney Mario, and Luca Carlone. Loc-nerf: Monte carlo localization using neural radiance fields. In *IEEE International Conference on Robotics and Automation (ICRA)*, pages 4018–4025. IEEE, 2023.

[29] Hidenobu Matsuki, Riku Murai, Paul HJ Kelly, and Andrew J Davison. Gaussian splatting slam. *arXiv preprint arXiv:2312.06741*, 2023.

[30] Ben Mildenhall, Pratul P. Srinivasan, Matthew Tancik, Jonathan T. Barron, Ravi Ramamoorthi, and Ren Ng. Nerf: Representing scenes as neural radiance fields for view synthesis. In *European Conference on Computer Vision (ECCV)*, 2020.

[31] Thomas Müller, Alex Evans, Christoph Schied, and Alexander Keller. Instant neural graphics primitives with a multiresolution hash encoding. *ACM Trans. Graph.*, 41(4):102:1–102:15, July 2022.

[32] Helen Oleynikova, Zachary Taylor, Marius Fehr, Roland Siegwart, and Juan Nieto. Voxblox: Incremental 3D Euclidean signed distance fields for on-board MAV planning. In *IEEE/RSJ International Conference on Intelligent Robots and Systems (IROS)*, 2017.

[33] Stanley Osher and Ronald P. Fedkiw. *Level Set Methods and Dynamic Implicit Surfaces*. Springer, New York, 2003. ISBN 978-0-387-22746-7.

[34] Jaesik Park, Qian-Yi Zhou, and Vladlen Koltun. Colored point cloud registration revisited. In *Proceedings of the IEEE international conference on computer vision*, pages 143–152, 2017.

[35] Nathan Ratliff, Matt Zucker, J Andrew Bagnell, and Siddhartha Srinivasa. Chomp: Gradient optimization techniques for efficient motion planning. In *2009 IEEE international conference on robotics and automation*, pages 489–494. IEEE, 2009.

[36] Antoni Rosinol, John J Leonard, and Luca Carlone. NeRF-SLAM: Real-Time Dense Monocular SLAM with Neural Radiance Fields. *arXiv preprint arXiv:2210.13641*, 2022.

[37] Ethan Rublee, Vincent Rabaud, Kurt Konolige, and Gary Bradski. Orb: An efficient alternative to sift or surf. In *2011 International conference on computer vision*, pages 2564–2571. Ieee, 2011.

[38] Radu Bogdan Rusu, Nico Blodow, and Michael Beetz. Fast point feature histograms (fpfh) for 3d registration. In *2009 IEEE international conference on robotics and automation*, pages 3212–3217. IEEE, 2009.

[39] John Schulman, Yan Duan, Jonathan Ho, Alex Lee, Ibrahim Awwal, Henry Bradlow, Jia Pan, Sachin Patil, Ken Goldberg, and Pieter Abbeel. Motion planning with sequential convex optimization and convex collision checking. *The International Journal of Robotics Research*, 33(9):1251–1270, 2014.

[40] Ioan A. Sucan, Mark Moll, and Lydia E. Kavraki. The Open Motion Planning Library. *IEEE Robotics & Automation Magazine*, 19(4):72–82, December 2012. doi: 10.1109/MRA.2012.2205651. <https://ompl.kavrakilab.org>.

[41] Edgar Sucar, Shikun Liu, Joseph Ortiz, and Andrew Davison. iMAP: Implicit mapping and positioning in real-time. In *Proceedings of the International Conference on Computer Vision (ICCV)*, 2021.

[42] Li Sun, Daniel Adolfsson, Martin Magnusson, Henrik Andreasson, Ingmar Posner, and Tom Duckett. Localising faster: Efficient and precise lidar-based robot localisation in large-scale environments. In *2020 IEEE international conference on robotics and automation (ICRA)*, pages 4386–4392. IEEE, 2020.

[43] M. Tancik, E. Weber, R. Li, B. Yi, T. Wang, A. Kristoffersen, J. Austin, K. Salahi, A. Ahuja, D. McAllister, A. Kanazawa, and E. Ng. Nerfstudio: A framework for neural radiance field development. In *SIGGRAPH*, 2023.

[44] George Terzakis and Manolis Lourakis. A consistently fast and globally optimal solution to the perspective-n-point problem. In *Computer Vision–ECCV 2020: 16th European Conference, Glasgow, UK, August 23–28, 2020, Proceedings, Part I 16*, pages 478–494. Springer, 2020.

[45] Mukun Tong, Charles Dawson, and Chuchu Fan. Enforcing safety for vision-based controllers via control barrier functions and neural radiance fields. In *IEEE International Conference on Robotics and Automation (ICRA)*, pages 10511–10517. IEEE, 2023.

[46] Inam Ullah, Yu Shen, Xin Su, Christian Esposito, and Chang Choi. A localization based on unscented kalman filter and particle filter localization algorithms. *IEEE Access*, 8:2233–2246, 2019.

[47] Shinji Umeyama. Least-squares estimation of transformation parameters between two point patterns. *IEEE Transactions on Pattern Analysis & Machine Intelligence*, 13(04):376–380, 1991.

[48] Prahlad Vadakkepat, Kay Chen Tan, and Wang Ming-Liang. Evolutionary artificial potential fields and their application in real time robot path planning. In *Proceedings of the 2000 congress on evolutionary computation. CEC00 (Cat. No. 00TH8512)*, volume 1, pages 256–263. IEEE, 2000.

[49] Jur Van den Berg, Ming Lin, and Dinesh Manocha. Reciprocal velocity obstacles for real-time multi-agent navigation. In *2008 IEEE international conference on robotics and automation*, pages 1928–1935. Ieee, 2008.

[50] Xiangyu Wu, Shuxiao Chen, Koushil Sreenath, and Mark W Mueller. Perception-aware receding horizon trajectory planning for multicopters with visual-inertial odometry. *IEEE Access*, 10:87911–87922, 2022.

[51] Chi Yan, Delin Qu, Dong Wang, Dan Xu, Zhigang Wang, Bin Zhao, and Xuelong Li. GS-SLAM: Dense visual slam with 3d gaussian splatting. *arXiv preprint arXiv:2311.11700*, 2023.

[52] Lin Yen-Chen, Pete Florence, Jonathan T Barron, Alberto Rodriguez, Phillip Isola, and Tsung-Yi Lin. Inerf: Inverting neural radiance fields for pose estimation. In *2021 IEEE/RSJ International Conference on Intelligent Robots and Systems (IROS)*, pages 1–8. IEEE, 2021.

and Systems (IROS), pages 1323–1330. IEEE, 2021.

[53] Vladimir Yugay, Yue Li, Theo Gevers, and Martin R Oswald. Gaussian-SLAM: Photo-realistic dense slam with gaussian splatting. *arXiv preprint arXiv:2312.10070*, 2023.

[54] Qi-bin Zhang, Peng Wang, and Zong-hai Chen. An improved particle filter for mobile robot localization based on particle swarm optimization. *Expert Systems with Applications*, 135:181–193, 2019.

[55] Zihan Zhu, Songyou Peng, Viktor Larsson, Weiwei Xu, Hujun Bao, Zhaopeng Cui, Martin R. Oswald, and Marc Pollefeys. Nice-SLAM: Neural implicit scalable encoding for slam. In *IEEE/CVF Conference on Computer Vision and Pattern Recognition (CVPR)*, June 2022.